Investigating the high field transport properties of Janus WSSe and MoSSe by DFT analysis and Monte Carlo simulations

Article *in* Journal of Applied Physics · April 2022

DOI: 10.1063/5.0088593

Yuh-Renn Wu
National Taiwan University

Journal of Applied Physics

Investigating the high field transport properties of Janus WSSe and MoSSe by DFT analysis and Monte Carlo simulations

Cite as: J. Appl. Phys. **131**, 144303 (2022); https://doi.org/10.1063/5.0088593
Submitted: 18 February 2022 • Accepted: 21 March 2022 • Published Online: 12 April 2022

Hsiu-Chi Pai and Yuh-Renn Wu

Journal of Applied Physics | ARTICLE | scitation.org/journal/jap

Investigating the high field transport properties of Janus WSSe and MoSSe by DFT analysis and Monte Carlo simulations

Cite as: J. Appl. Phys. **131**, 144303 (2022); doi: 10.1063/5.0088593
Submitted: 18 February 2022 · Accepted: 21 March 2022 ·
Published Online: 12 April 2022

View Online Export Citation CrossMark

Hsiu-Chi Pai[1] and Yuh-Renn Wu[1,2,a)]

AFFILIATIONS

[1]Graduate Institute of Photonics and Optoelectronics and Department of Electrical Engineering, National Taiwan University, Taipei 10617, Taiwan
[2]Electronic and Optoelectronic System Research Laboratories, Industrial Technology Research Institute, Hsinchu 31040, Taiwan

[a)]**Author to whom correspondence should be addressed:** yrwu@ntu.edu.tw

ABSTRACT

Janus transition metal dichalcogenides with out-of-plane structural asymmetry have attracted increasing attention due to their exceptional potential in electronic and optical applications. In this study, we systematically investigated the electron–phonon interactions and related transport properties in monolayer Janus MoSSe and WSSe using the density-functional formalism. The electron–phonon scattering rates were obtained using Fermi's golden rule and extended to the extraction of the effective deformation potential constants for further Monte Carlo treatment. From the results of the Monte Carlo analysis, we found that WSSe provides better performance with higher low-field mobility, while MoSSe shows a higher peak velocity at higher fields. In our results, both MoSSe and WSSe seem to be competitive with other previously studied 2D materials. These predictions provide a systematic perspective on the potential of Janus WSSe and MoSSe for electronic applications.

I. INTRODUCTION

Since the great success of the first graphene exfoliation in 2004,[1] two-dimensional (2D) materials such as silicene,[2–5] silicane,[6–9] germanene,[3,6,10] phosphorene,[11–16] and monolayer transition metal dichalcogenides (TMDs)[17–19] have attracted considerable attention in various fields. Among these 2D materials, TMDs are among the most researched because of their tunable bandgap, ability to form ultrathin structures, and unique electronic, optical, and mechanical properties.[20–23] In particular, the existence of an intrinsic direct bandgap in TMDs has made this class of materials appealing for applications in field-effect transistors (FETs).[24,25] The atomistic configuration of 2D monolayer TMDs is a sandwich structure consisting of one transition-metal-atom layer located between two chalcogen-atom layers made from the same element. If the two chalcogen-atom layers are different, then Janus 2D monolayer TMDs (JTMDs) will be formed (Fig. 1).

In the last few years, novel JTMDs have attracted increasing attention, and they have gradually started to serve as a new interesting type of 2D semiconductor due to their potential applications in quantum science, spintronics, and energy conservation.[26] Janus monolayer MoSSe has been successfully synthesized using different experimental methods. For example, Lu *et al.*[27] and Zhang *et al.*[28] controlled the reaction conditions to substitute one of the chalcogen atom layers within $MoS_2/MoSe_2$ for another chalcogen atom layer through a chemical vapor deposition method. An intrinsic vertical piezoelectric response and vertical dipoles originating from the out-of-plane structural asymmetry are observed in JTMDs.[29,30] In addition, bandgap engineering, van der Waals heterostructures, solar water-splitting, and photocurrent responses based on Janus materials have also recently been investigated.[31–37] Previous theoretical calculations for Janus MoSSe and WSSe have provided clear evidence of a lack of imaginary frequencies in their phonon spectra, confirming their stability and presenting the possibility of their experimental manufacture.[33,38,39] Other theoretical studies have predicted the intrinsic electron or hole mobility in Janus MoSSe[40] and WSSe[41] using an acoustic-phonon-limited approach.[42]

Nonetheless, there has as yet been little research conducting systematic transport analysis of JTMDs, and their field-dependent

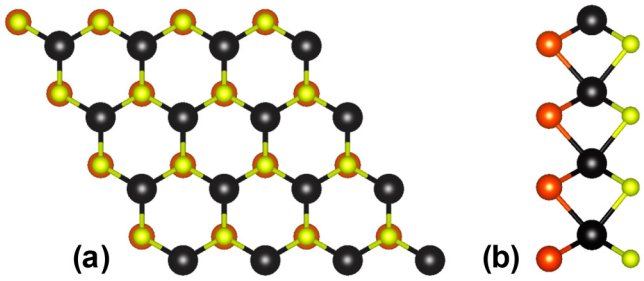

FIG. 1. (a) Top and (b) side views of the crystal structure of a MoSSe monolayer. The large black balls represent Mo atoms, the medium-sized orange balls represent Se atoms, and the small yellow balls represent S atoms.

transport properties are still unclear. In this study, we investigated the intrinsic electron–phonon mobility of Janus monolayer MoSSe and WSSe from low to high field strengths by taking advantage of first-principles calculations based on density functional theory (DFT) and Monte Carlo carrier-transport simulations. The analysis was also further extended to estimating the effective deformation potential constants for a simplified treatment. We believe that our results provide a systematic perspective on these materials and their potential electronic applications, and they offer appealing alternatives to conventional semiconductors in electronic applications with ultrasmall dimensions.

II. COMPUTATIONAL DETAILS

The work reported here was performed in the DFT framework as implemented in the QUANTUM ESPRESSO package[43] using norm-conserving Vanderbilt[44] pseudopotentials with the generalized gradient approximation (GGA) for the exchange–correlation functional. In our approach, the geometry is optimized until the atomic forces decrease to a value less than 0.015 eV/Å and the dipole correction is applied to both MoSSe and WSSe to cancel the artificial electric field due to their asymmetric slab structures. The vacuum region is set as 20 Å to minimize the interactions between adjacent supercells. We initially calculate the electronic band and phonon energies using an $18 \times 18 \times 1$ k-point mesh and a $6 \times 6 \times 1$ q-point mesh with a self-consistent threshold of 10^{-13} Ry to avoid nonphysical imaginary frequencies for the low-energy acoustic phonons. The matrix element for an electron in an initial state with wave vector $\mathbf{k}$ in band m to a final state with wave vector $\mathbf{k}+\mathbf{q}$ in band n is given by

$$g^{\nu}_{mn}(\mathbf{k},\mathbf{q}) = \langle \psi_{m,\mathbf{k}+\mathbf{q}} | \partial_{\mathbf{q}\nu} V | \psi_{n,\mathbf{k}} \rangle, \tag{1}$$

where m and n are the initial and final electron band indices with wave vectors $\mathbf{k}$ and $\mathbf{k}+\mathbf{q}$, respectively, and $\partial_{\mathbf{q},\nu}$ is the derivative of the self-consistent potential associated with a phonon of wave vector $\mathbf{q}$ in branch ν. The matrix elements are evaluated over a fine grid of $400 \times 400 \times 1$ q points to obtain the imaginary part of the self-energy within the EPW (electron–phonon coupling using Wannier functions) code.[45] The electron self-energy and electron–phonon scattering rates are given by

$$\Sigma^{\text{e-ph}}_{n\mathbf{k}} = \sum_{\mathbf{q},\nu,m} W_{\mathbf{q}} \left| g^{\nu}_{mn}(\mathbf{k},\mathbf{q}) \right|^2 \left[\frac{n(\omega_{\mathbf{q},\nu}) + f(\varepsilon_{m,\mathbf{k}+q})}{\varepsilon_{n,\mathbf{k}} - \varepsilon_{m,\mathbf{k}+\mathbf{q}} + \omega_{\mathbf{q},\nu} - i\eta} + \frac{n(\omega_{\mathbf{q},\nu}) + 1 + f(\varepsilon_{m,\mathbf{k}+q})}{\varepsilon_{n,\mathbf{k}} - \varepsilon_{m,\mathbf{k}+\mathbf{q}} - \omega_{\mathbf{q},\nu} - i\eta} \right], \tag{2}$$

$$(\tau^{\text{e-ph}}_{n\mathbf{k}})^{-1} = 2[\Im\mathfrak{m}(\Sigma^{\text{e-ph}}_{n\mathbf{k}})]/\hbar, \tag{3}$$

where $W_{\mathbf{q}}$ are the Brillouin zone weights associated with each $\mathbf{q}$, f is the Fermi occupancy function, $\varepsilon_{\mathbf{k},\mathbf{q}}$ is the electron energy in band n and state $\mathbf{k}$, $\hbar\omega_{\mathbf{q},\nu}$ is the phonon energy in band ν and state $\mathbf{q}$, and n is the Bose occupation factor. In our numerical calculations, the energy-conserving δ-function is approximated by a Gaussian of width 0.005 eV. For further Monte Carlo transport calculations, the first-principles result is approximated by the deformation potential (DP) model[46,47] to describe the electron–phonon interactions and the multivalley transition behavior,

$$W_{\text{ac}}(k) = \frac{\pi k_B T D_0^2}{\hbar \rho v_{\text{ac}}^2} N_{\text{2D}}(E_k), \tag{4}$$

$$W^{\text{abs/emi}}_{\text{ac/op}}(k) = \frac{\pi D^2_{\text{ac/op}}}{2\rho\omega} \left[n(\omega) + \frac{1}{2} \mp \frac{1}{2} \right] N_{\text{2D}}(E_k \pm \hbar\omega), \tag{5}$$

where v_{ac} is the sound velocity, D_0 is the deformation potential of an intravalley acoustic phonon, $D_{\text{ac/op}}$ represents the deformation potential of intervalley acoustic phonons and intra/intervalley optical phonons, ρ is the mass density, and N_{2D} is the 2D density of states.

The DFT and density functional perturbation theory results provide the physical details necessary to obtain the transport characteristics using the Monte Carlo method, which is a statistical approach that is used to simulate random events. Figure 2(a) illustrates electron transport in a material accelerated under an electric force. During the flight, an electron will collide with phonons and then scatter with changing momentum and velocity until the next scattering occurs. Given that the whole process of the flight intervals between scattering events and the state after scattering are probability issues, the Monte Carlo method is a practical approach to simulating this kind of real physical phenomenon. The detailed steps of the Monte Carlo method are depicted in Fig. 2(b). The free-flight time, scattering events, and final state of electrons during the flight are determined by generating random numbers; hundreds of cycles of the process can be conducted to obtain the average carrier mobilities and velocities under a certain electric field. In our simulations, the total flight for each electron was set to 10^5 nm to make sure that a steady state was reached and the results were not affected by the bias of random numbers. Finally, field-dependent velocities and mobilities were extracted.

III. RESULTS AND DISCUSSION

The DFT calculations of monolayer MoSSe and WSSe show direct bandgaps with the conduction band (CB) minimum and

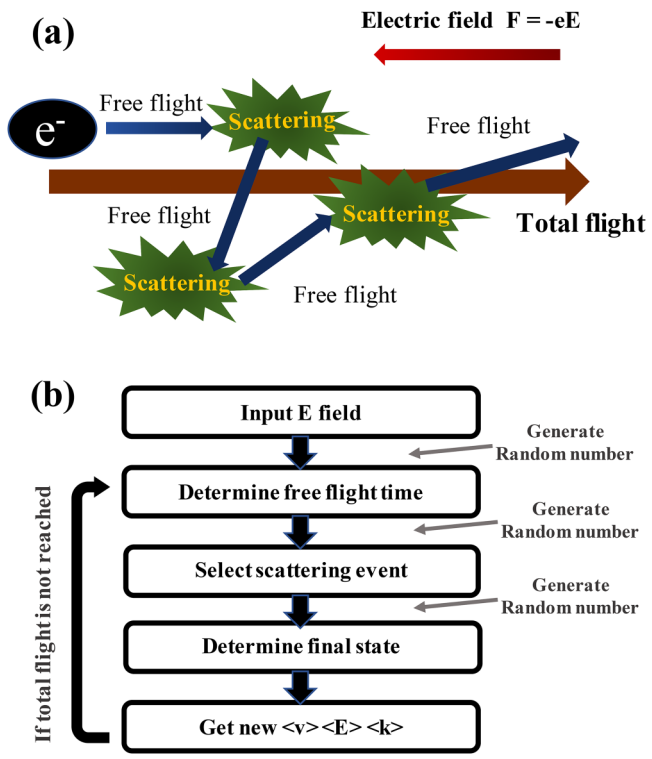

FIG. 2. (a) Schematic diagram of carrier transport in the material. (b) Flow chart of Monte Carlo method.

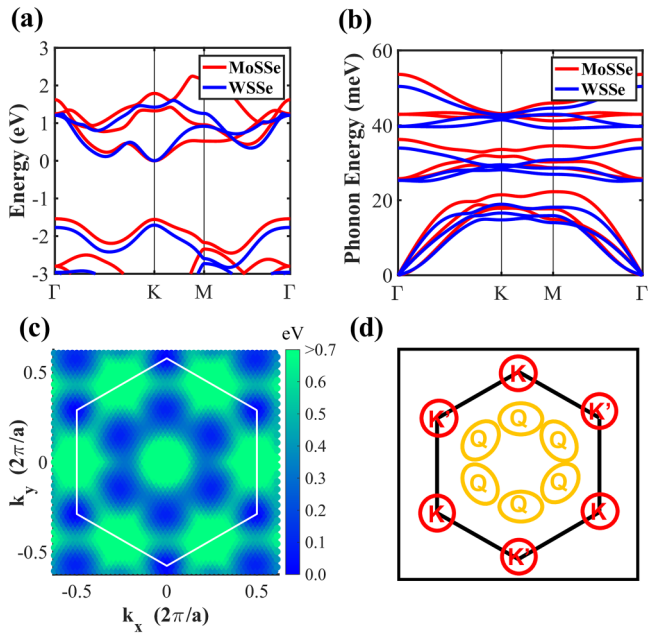

FIG. 3. (a) Electronic and (b) phononic dispersion of monolayer MoSSe and WSSe in the FBZ. The CB minimum at the *K* point serves as the reference of the energy scale (i.e., the point of zero energy). (c) CB in colormap view; the vertical color bar denotes the carrier energy with respect to the reference. (d) Schematic diagram of the *K*–*Q* valley distribution.

valence band maximum at the *K* point in momentum space. This result is consistent with the results of previous theoretical calculations.[48–50] For the CB, a satellite energy minimum is also observed along the *K*–Γ axis near the halfway point that is often called the *Q* valley, which is six in number within the first Brillouin zone (FBZ), as depicted in Figs. 3(a), 3(c), and 3(d). Table I summarizes the optimized lattice constants, bandgaps, *Q*–*K* separation energies for the CB (E_{KQ}), the corresponding effective masses and low-field mobilities for Janus monolayer MoSSe, WSSe, and the four other symmetric monolayer TMDs. Notably, the estimates for E_{KQ} in this study are quite sizable (around 110 and 260 meV) compared to those of the general TMDs discussed in previous reports, such as MoS_2, WS_2, $MoSe_2$, and WSe_2;[5,51] the values for these materials are in a range (<85 meV) that could significantly affect electron transport via intervalley scattering even under low-bias conditions. It is well known that the bandgap obtained by GGA is typically smaller than the method from the hybrid functional method.[30,35] However, the actual bandgap needs more experimental result to verify in the near future. Furthermore, in the transport study, especially the high field transport, the more important factors are the valley separation of K and Q valley and the effective mass, which is believed that GGA can provide a certain accuracy and reliability on these parameters.[52] Other than that, the bandgap is mainly affecting the optoelectronic properties or the inversion of the channel, which is not the focus of this paper.

A comparison with similar calculations in the literature[53–55] suggests that the intervalley separation energies are sensitive to the details of the first-principles approach including the selection of pseudopotentials. In particular, application of the local density approximation tends to predict smaller values, while conversely, the GGA predicts higher values. This inconsistency requires further clarification through accurate experimental determinations. As for the effective masses, both the longitudinal and transverse directions are necessary for the *Q* valleys due to their anisotropic nature. Those listed in Table I represent the geometric mean values, and these also appear to be very close to the conductivity effective masses.

TABLE I. The calculated lattice constant, bandgap, and *K*–*Q* valley separation, the effective masses at relevant energy valleys, and low-field mobility for Janus monolayer MoSSe, WSSe, and the four other symmetric monolayer TMDs in this study. The effective masses are given in units of electron rest mass m_0.

	a (Å)	E_g (eV)	ΔE_{KQ} (meV)	m_K (m_0)	m_Q (m_0)	μ (cm^2/V s)
MoSSe	3.25	1.56	227	0.51	0.81	152
WSSe	3.25	1.71	110	0.33	0.65	238
MoS_2	3.18	1.69	261	0.48	0.76	181
WS_2	3.19	1.82	213	0.30	0.60	382
$MoSe_2$	3.32	1.43	156	0.53	0.80	146
WSe_2	3.32	1.54	123	0.34	0.64	257

Figure 3(b) shows the phonon dispersions of the MoSSe and WSSe monolayers along a high-symmetry path; these agree well with previous results.[27,56,57] The three acoustic and six optical phonon branches are observed based on the three atoms in the unit cell. The longitudinal acoustic (LA) and transversal acoustic (TA) branches show linearity near the Γ point, while the out-of-plane acoustic (ZA) branch deviates strongly from a parabolic law. Similar behavior can be observed in many 2D materials.[58–61] The LA phonon dispersion relation is well approximated by the sound velocity in the long-wavelength limit, with 4.9×10^5 cm/s for WSSe and 5.6×10^5 cm/s for MoSSe. From MoSSe to WSSe, the acoustic modes become softened and the optical branches move toward a lower energy overall, meaning reduced group velocities.

Figures 4(a)–4(d) show the electron–phonon interaction matrix elements for the initial electron state at $\mathbf{k} = K$ for TA and LA phonon modes. The matrix elements for $\mathbf{k} = K$ demonstrate a threefold-rotational symmetry (i.e., 120°). As can be seen from the figures, the TA phonon mode for both materials indicates strong electron–phonon interaction at symmetry points Q in phonon momentum space (denoted as $\mathbf{q} = Q$ for simplicity), which implies the induction of the electron transition from the K to the Q valley with phonon energy at $\mathbf{q} = Q$. As for the LA phonon mode, the strongest electron–phonon interaction lies at $\mathbf{q} = M$, implying the induction of the electron transition from the K to the Q valley with phonon energy at $\mathbf{q} = M$. Figures 4(e) and 4(f) show the electron–phonon interaction matrix elements for the initial electron state at $\mathbf{k} = Q$ along the K–Γ axis for LA phonon modes. However, the matrix elements for $\mathbf{k} = Q$ show reflection symmetry, and the strongest electron–phonon interaction, located at $\mathbf{q} = K$, can be associated with the electron scattering from Q to Q with phonon energy at $\mathbf{q} = K$. The characteristics of the electron–phonon interaction matrix elements for MoSSe and WSSe are nearly identical,

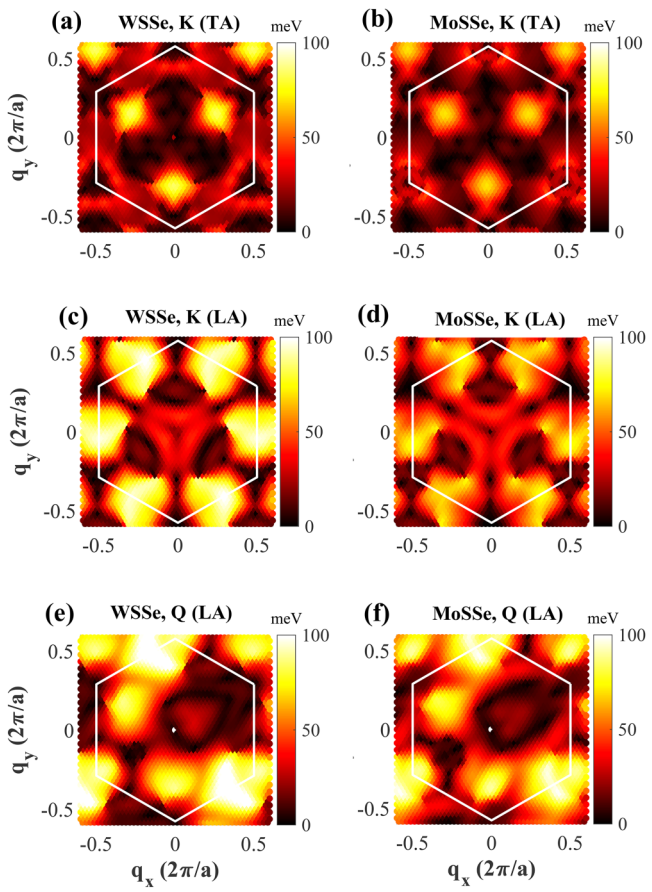

FIG. 4. (a)–(d) Electron–phonon interaction matrix elements for TA and LA phonon modes $|g^{\nu}_{mn}(\mathbf{k}, \mathbf{q})|$ (in units of meV) from the EPW calculation in WSSe and MoSSe with $\mathbf{k}$ at the CB minimum K point as a function of the phonon wave vector $\mathbf{q}$. Panels (e) and (f) show the electron–phonon interaction matrix elements for LA phonon modes with k at the Q point along the K–Γ axis.

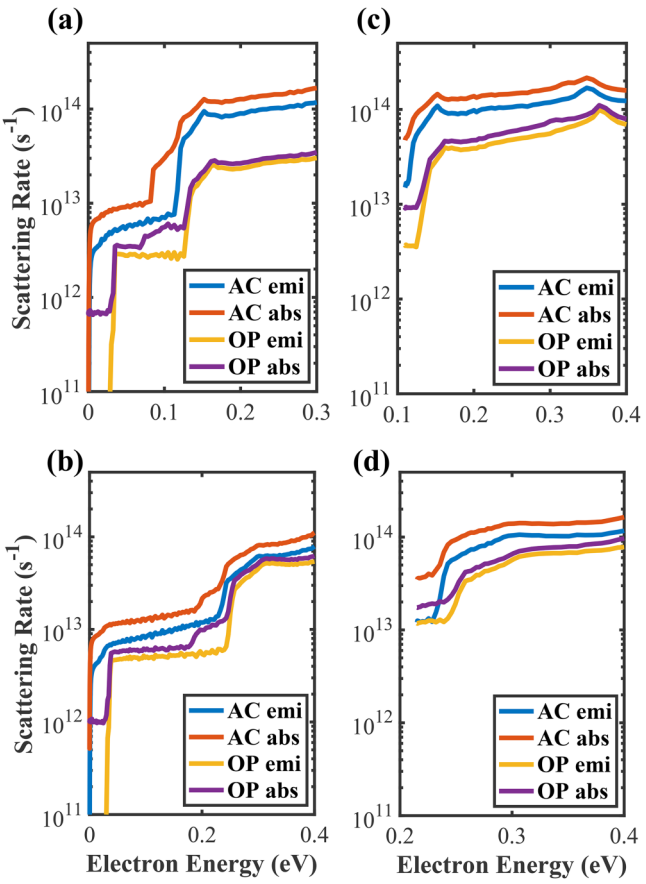

FIG. 5. Scattering rates of K-valley electrons in (a) WSSe and (b) MoSSe via emission and absorption of phonons calculated at 300 K, where the wave vector $\mathbf{k}$ is assumed to be along the K–Γ axis. The scattering rates of Q-valley electrons are given in (c) and (d), where the wave vector $\mathbf{k}$ is assumed to be along the Q–Γ axis. The reference of energy scales is adjusted accordingly to the corresponding K–Q energy separation. The abbreviations AC and OP denote acoustic and optical phonons, respectively.

indicating similar electron transitions in the scattering rates of the related modes.

The electron–phonon scattering rates are calculated as a function of electron energy, which is directly connected to the imaginary part of the electron self-energy, as mentioned in Eq. (3). For a more quantitative comparison, the contributions of acoustic and optical modes are summed as the total emission and absorption scattering rates. Figures 5(a) and 5(b) give the rates for electrons in the K valleys at 300 K, while the results for Q-valley electrons are shown in Figs. 5(c) and 5(d); the wave vector $\mathbf{k}$ of the initial electronic state is chosen along the K–Γ and Q–Γ axes, respectively. As can be seen from these figures, acoustic phonons dominate the initial energy, which is consistent with their large coupling strength. The steps in the curves indicate either the onset of intervalley scattering or optical phonon emission. For WSSe, the abrupt increase observed in the rate of acoustic phonons at ~100 meV can be attributed to the above-mentioned strong K-to-Q transition; for MoSSe, the abrupt increase is observed at around 220 meV. The difference in the discontinuity of the curves obviously results from the variation of the E_{KQ} value. The same characteristic can also be seen in the rates of optical phonons. Like many other TMDs, the rates in acoustic phonons dominate at lower electron energies due to the strong intravalley scattering in K valleys,[53–55] and the rates in optical phonons increase at higher electron energies. The large density of states in the Q valleys (corresponding to the large effective masses) makes the contribution of this scattering even more prominent.

For further Monte Carlo simulations, the *ab initio* results were fitted by the DP analytical model, as mentioned above in Eqs. (4) and (5). The extracted DP constants for each transition process in the materials considered and the phonon momentum involved (in the form of its location in momentum space) are listed in Table II, in which each phonon momentum is the average of the relevant phonon modes. Using these fitted results, the relationship between the mobility and velocity and the field can be obtained by Monte Carlo simulation.

As shown in Fig. 6(a), the estimated intrinsic mobilities are approximately 238 $cm^2/V\,s$ for WSSe and 152 $cm^2/V\,s$ for MoSSe. The peak velocities reached are approximately 2.5×10^6 and 3.2×10^6 cm/s for WSSe and MoSSe, respectively. Notably, we

TABLE II. Estimated deformation potential constants of Janus monolayer MoSSe and WSSe. The first column indicates the electronic transition with corresponding phonon momentum. The symbols ac and op denote acoustic and optical phonons, respectively. The phonon energies ($\hbar\omega$ in meV) in the third and fifth columns are the averages of the phonon energies of the relevant modes. The second and fourth columns list the deformation potential for MoSSe and WSSe. The first-order deformation potential D_1 are given in eV unit while 10^8 eV/cm correspond to the zeroth-order deformation potential D_0.

Transition	MoSSe D_1 (eV)	Phonon ($\hbar\omega$) (meV)	WSSe D_1 (eV)	Phonon ($\hbar\omega$) (meV)
$K \to K(\Gamma)$, ac	5.1	0	5.8	0
$Q \to Q(\Gamma)$, ac	3.7	0	4.8	0
Transition	D_0 (10^8 eV/cm)	Phonon ($\hbar\omega$) (meV)	D_0 (10^8 eV/cm)	Phonon ($\hbar\omega$) (meV)
$K \to K(\Gamma)$, op	3.6	30.62	5.5	30.62
$K \to K(K)$, ac	1.8	19.18	1.7	16.76
$K \to K(K)$, op	3.3	31.88	3.5	30.38
$K \to Q(Q)$, ac	2.0	14.95	1.7	12.79
$K \to Q(Q)$, op	5.2	32.51	3.4	30.39
$K \to Q(M)$, ac	3.7	18.30	5.4	16.02
$K \to Q(M)$, op	6.2	31.89	4.6	30.44
$Q \to Q(\Gamma)$, op	6.4	30.62	7.9	30.62
$Q \to Q(Q)$, ac	4.8	14.95	5.5	12.79
$Q \to Q(Q)$, op	4.6	32.51	4.6	30.39
$Q \to Q(M)$, ac	2.5	18.30	2.2	16.02
$Q \to Q(M)$, op	4.9	31.89	4.3	30.44
$Q \to Q(K)$, ac	3.0	19.18	4.5	16.76
$Q \to Q(K)$, op	5.4	31.88	2.9	30.38
$Q \to K(Q)$, ac	1.2	14.95	1.5	12.79
$Q \to K(Q)$, op	5.1	32.51	3.4	30.39
$Q \to K(M)$, ac	3.3	18.30	6.6	16.02
$Q \to K(M)$, op	6.0	31.89	5.4	30.44

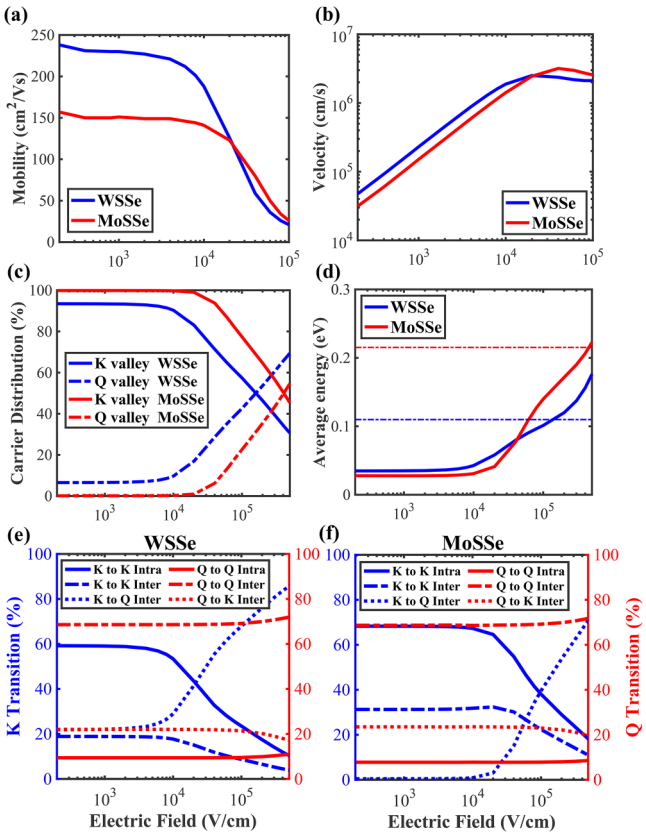

FIG. 6. (a) Mobility, (b) drift velocity, (c) carrier distribution of K–Q valleys, and (d) average electron energy vs electric field in monolayer WSSe and MoSSe obtained by Monte Carlo calculations. Panels (e) and (f) illustrate the percentage of K–Q electron transition for monolayer WSSe and MoSSe, respectively.

observe negative differential mobility at the field after around 10^4 V/cm for both WSSe and MoSSe [see Fig. 6(b)]. This is due to the significant transfer of electrons to Q valleys (large effective, mass hence lower velocity) at high fields. Because of the large E_{KQ} value of MoSSe, there are nearly no Q electrons until around 10^4 V/cm, suggesting the low impact of the Q-valley effect at low fields; while there are some Q electrons for WSSe at low fields, as shown in Fig. 6(c). It can also be clearly seen from the transition trend in Figs. 6(e) and 6(f) that the above-mentioned phenomenon can be attributed to the decrease in K intravalley transitions and the significant surge in K-to-Q intervalley transition for both materials above 10^4 V/cm. The steady-state electron distribution in k space is shown in Figs. 7(a)–7(c) for various values of the strength of the applied electric field. At low field, the electrons mostly populate the K valleys; however, at higher fields, the electrons gain enough energy to scatter to the satellite Q valleys.

To reveal the enhancement of the strain effect on the electron-transport properties in the materials discussed, we consider MoSSe as a prototypical example and examine its band structures under different biaxial strains. As shown in Fig. 8(a), the curvatures of the K valleys are nearly identical, indicating that the effective masses at the band edge remain practically invariant. We also observe that the energy levels of Q valleys increase if a tensile strain is applied and decrease if a compressive strain is applied. For phonon dispersions [Fig. 8(b)], there is no imaginary frequency existing in the acoustic mode, suggesting the well-optimized stable structures under these applied strains. The parabolicity in the first acoustic mode (ZA) near gamma point slightly turns linear as the strain increases positively, and the overall phonon energies become lower. These results are consistent with other theoretical calculations.[36,62,63] The calculated total scattering rates for each strained case are depicted in Fig. 8(c). We can almost say that if the K valleys remain at the CB minimum, then the biaxial strain will only affect the onset energy of the K-to-Q electron transition. Clearly, 1% compressive strain gives a higher rate at low energy, and this results from the energy alignment of the K and Q valleys; to the best of our knowledge, higher compression will make Q valleys

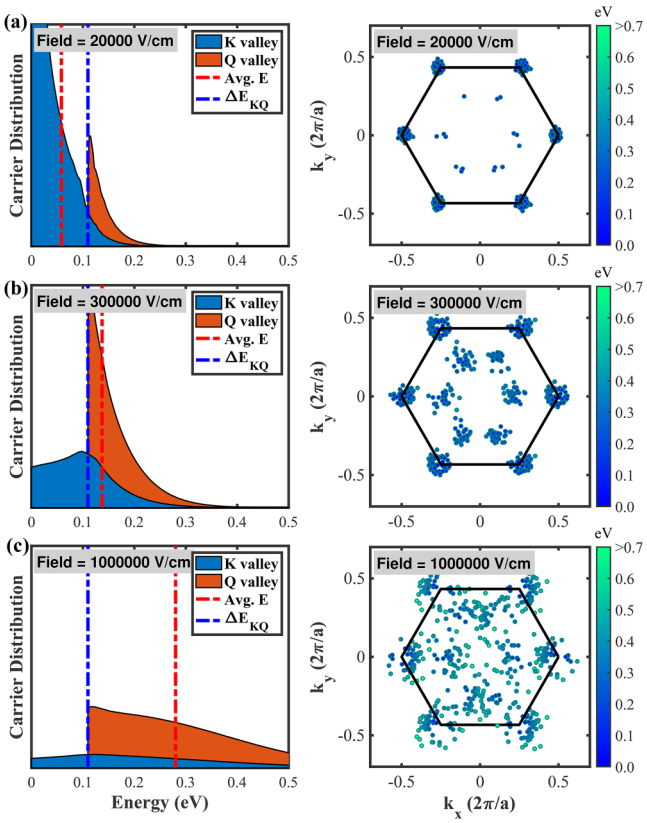

FIG. 7. (a)–(c) Room-temperature distribution of electrons in the FBZ under low-to-high electric field strengths for WSSe. At low fields, the electrons mostly populate the K valleys. With increasing electric field magnitude, the electrons gain enough energy to scatter to the satellite Q valleys.

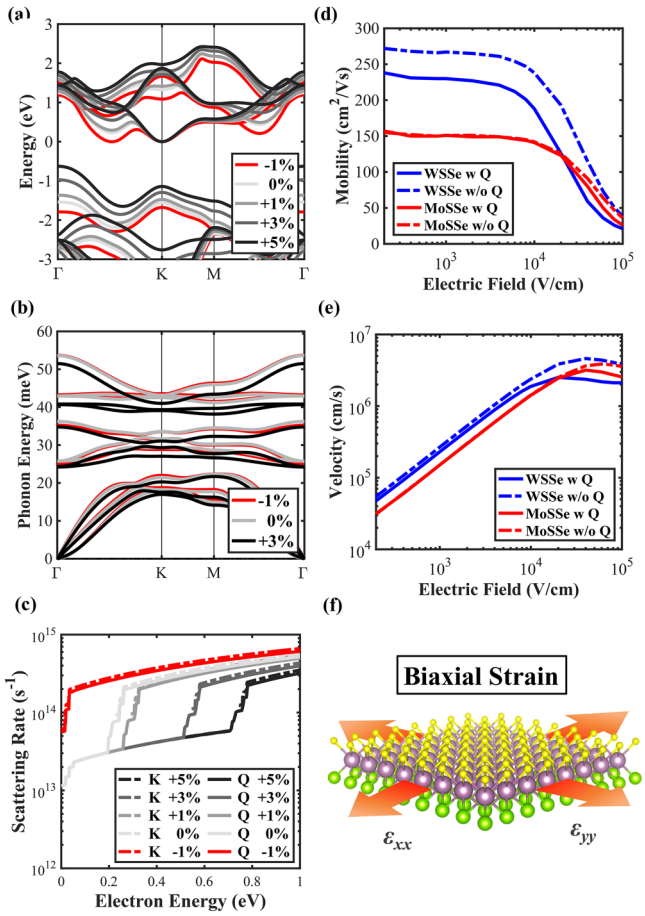

FIG. 8. (a)–(c) MoSSe band structures, phonon dispersions, and scattering rates with different biaxial strains. (d)–(e) Field-dependent mobilities and velocities when the Q valleys are not considered. (f) Schematic illustration of the material under biaxial strain.

become the minimum band, leading to more valleys at low energy levels (from two K valleys to six Q valleys).

Since the tensile strain increases the Q-valley energy level, we are interested in the result when the influence of Q valleys is neglected. As shown in Figs. 8(d) and 8(e), the estimated mobility when not accounting for Q-valley effects is around 270 cm^2/V s for WSSe, and it is nearly the same for MoSSe. The peak velocity increases from 2.5×10^6 to 4.6×10^6 cm/s for WSSe and from 3.2×10^6 to 3.9×10^6 cm/s for MoSSe. It is clear that the E_{KQ} value of WSSe is still in the range that affects electron transport, but this is not the case for MoSSe.

Finally, we compare the mobilities of Janus MoSSe and WSSe with symmetric TMDs, as listed in the last column of Table I. Of the four symmetric TMD materials, WS_2 and $MoSe_2$ appears to provide the most and the least promising performances, respectively, while MoS_2 and WSe_2 are in between. The W compounds may be electrically less resistive than those of Mo with lower scattering rates. Between the two chalcogens, S atoms appears to scatter the electrons less strongly through the interaction with the phonons.[51] It is worth noting that the results of MoSSe and WSSe are not expected to be the average performance of $MoS_2(WS_2)$ and $MoSe_2(WSe_2)$. Due to the breaking out-of-plane symmetry, the divergence of vertical structural displacements dramatically affect electronic transport because electrons are allowed to strongly couple with the out-of-plane phonons.[64] Thus, unlike the symmetric TMDs, MoSSe and WSSe suffer much performances degradation due to higher scattering rates originated from this additional scattering source. While even that, MoSSe and WSSe are still predicted with competitive transport performances and serve as a potential alternative materials for electronic devices.

IV. CONCLUSION

This study used first-principles calculations combined with Monte Carlo transport simulations to analyze the intrinsic electron–phonon transport properties in MoSSe and WSSe. Of these two materials, WSSe appears to provide better performance than MoSSe. That being said, both materials show competitive mobilities and sizable bandgaps that are suitable for FET applications. Because the transport properties are highly sensitive to variations in the band structure in the meV range and discrepancies originating from the accuracy of the DFT results, the results of these calculations in 2D materials still require further confirmation by experimental evidence. The first-principles method can at best provide a relatively convincing and systematic analysis of the carrier mobility.

ACKNOWLEDGMENTS

This work was supported by the Ministry of Science and Technology under Grant Nos. MOST-109-2221-E-00-196-MY2, MOST-110-2622-8-002-014, and 111-2923-E-002-009.

AUTHOR DECLARATIONS

Conflict of Interest

The authors have no conflicts to disclose.

DATA AVAILABILITY

The data that support the findings of this study are available from the corresponding author upon reasonable request.

REFERENCES

[1]K. S. Novoselov, A. K. Geim, S. V. Morozov, D. Jiang, Y. Zhang, S. V. Dubonos, I. V. Grigorieva, and A. A. Firsov, "Electric field effect in atomically thin carbon films," Science **306**, 666–669 (2004).
[2]P. Vogt, P. De Padova, C. Quaresima, J. Avila, E. Frantzeskakis, M. C. Asensio, A. Resta, B. Ealet, and G. Le Lay, "Silicene: Compelling experimental evidence for graphenelike two-dimensional silicon," Phys. Rev. Lett. **108**, 155501 (2012).
[3]N. J. Roome and J. D. Carey, "Beyond graphene: Stable elemental monolayers of silicene and germanene," ACS Appl. Mater. Interfaces **6**, 7743–7750 (2014).
[4]L. Tao, E. Cinquanta, D. Chiappe, C. Grazianetti, M. Fanciulli, M. Dubey, A. Molle, and D. Akinwande, "Silicene field-effect transistors operating at room temperature," Nat. Nanotechnol. **10**, 227–231 (2015).
[5]X. Li, J. T. Mullen, Z. Jin, K. M. Borysenko, M. B. Nardelli, and K. W. Kim, "Intrinsic electrical transport properties of monolayer silicene and MoS_2 from first principles," Phys. Rev. B **87**, 115418 (2013).
[6]M. Houssa, E. Scalise, K. Sankaran, G. Pourtois, V. Afanas' Ev, and A. Stesmans, "Electronic properties of hydrogenated silicene and germanene," Appl. Phys. Lett. **98**, 223107 (2011).
[7]O. D. Restrepo, R. Mishra, J. E. Goldberger, and W. Windl, "Tunable gaps and enhanced mobilities in strain-engineered silicane," J. Appl. Phys. **115**, 033711 (2014).
[8]K. L. Low, W. Huang, Y.-C. Yeo, and G. Liang, "Ballistic transport performance of silicane and germanane transistors," IEEE Trans. Electron Devices **61**, 1590–1598 (2014).
[9]M. M. Khatami, G. Gaddemane, M. L. Van de Put, M. V. Fischetti, M. K. Moravvej-Farshi, M. Pourfath, and W. G. Vandenberghe, "Electronic transport properties of silicane determined from first principles," Materials **12**, 2935 (2019).
[10]M. Dávila, L. Xian, S. Cahangirov, A. Rubio, and G. Le Lay, "Germanene: A novel two-dimensional germanium allotrope akin to graphene and silicene," New J. Phys. **16**, 095002 (2014).
[11]A. Castellanos-Gomez, L. Vicarelli, E. Prada, J. O. Island, K. Narasimha-Acharya, S. I. Blanter, D. J. Groenendijk, M. Buscema, G. A. Steele, J. Alvarez *et al.*, "Isolation and characterization of few-layer black phosphorus," 2D Mater. **1**, 025001 (2014).
[12]L. Li, Y. Yu, G. J. Ye, Q. Ge, X. Ou, H. Wu, D. Feng, X. H. Chen, and Y. Zhang, "Black phosphorus field-effect transistors," Nat. Nanotechnol. **9**, 372–377 (2014).
[13]H. Liu, A. T. Neal, Z. Zhu, Z. Luo, X. Xu, D. Tománek, and P. D. Ye, "Phosphorene: An unexplored 2D semiconductor with a high hole mobility," ACS Nano **8**, 4033–4041 (2014).
[14]Y. Cao, A. Mishchenko, G. Yu, E. Khestanova, A. Rooney, E. Prestat, A. Kretinin, P. Blake, M. B. Shalom, C. Woods *et al.*, "Quality heterostructures from two-dimensional crystals unstable in air by their assembly in inert atmosphere," Nano Lett. **15**, 4914–4921 (2015).
[15]R. A. Doganov, S. P. Koenig, Y. Yeo, K. Watanabe, T. Taniguchi, and B. Özyilmaz, "Transport properties of ultrathin black phosphorus on hexagonal boron nitride," Appl. Phys. Lett. **106**, 083505 (2015).
[16]N. Gillgren, D. Wickramaratne, Y. Shi, T. Espiritu, J. Yang, J. Hu, J. Wei, X. Liu, Z. Mao, K. Watanabe *et al.*, "Gate tunable quantum oscillations in air-stable and high mobility few-layer phosphorene heterostructures," 2D Mater. **2**, 011001 (2015).
[17]K. F. Mak, C. Lee, J. Hone, J. Shan, and T. F. Heinz, "Atomically thin MoS_2: A new direct-gap semiconductor," Phys. Rev. Lett. **105**, 136805 (2010).
[18]B. Radisavljevic, A. Radenovic, J. Brivio, V. Giacometti, and A. Kis, "Single-layer MoS_2 transistors," Nat. Nanotechnol. **6**, 147–150 (2011).

[19]S. Larentis, B. Fallahazad, and E. Tutuc, "Field-effect transistors and intrinsic mobility in ultra-thin $MoSe_2$ layers," Appl. Phys. Lett. **101**, 223104 (2012).
[20]J.-K. Huang, J. Pu, C.-L. Hsu, M.-H. Chiu, Z.-Y. Juang, Y.-H. Chang, W.-H. Chang, Y. Iwasa, T. Takenobu, and L.-J. Li, "Large-area synthesis of highly crystalline WSe_2 monolayers and device applications," ACS Nano **8**, 923–930 (2014).
[21]S. Manzeli, D. Ovchinnikov, D. Pasquier, O. V. Yazyev, and A. Kis, "2D transition metal dichalcogenides," Nat. Rev. Mater. **2**, 147 (2017).
[22]C. Tan, Z. Lai, and H. Zhang, "Ultrathin two-dimensional multinary layered metal chalcogenide nanomaterials," Adv. Mater. **29**, 1701392 (2017).
[23]X. Zhang, Z. Lai, Q. Ma, and H. Zhang, "Novel structured transition metal dichalcogenide nanosheets," Chem. Soc. Rev. **47**, 3301–3338 (2018).
[24]P.-F. Chen, E. Chen, and Y.-R. Wu, "Design of monolayer MoS_2 nanosheet transistors for low-power applications," IEEE Trans. Electron Devices **69**, 358–363 (2021).
[25]T. Pandey, D. S. Parker, and L. Lindsay, "*Ab initio* phonon thermal transport in monolayer InSe, GaSe, GaS, and alloys," Nanotechnology **28**, 455706 (2017).
[26]M. Yagmurcukardes, Y. Qin, S. Ozen, M. Sayyad, F. M. Peeters, S. Tongay, and H. Sahin, "Quantum properties and applications of 2D Janus crystals and their superlattices," Appl. Phys. Rev. **7**, 011311 (2020).
[27]A.-Y. Lu, H. Zhu, J. Xiao, C.-P. Chuu, Y. Han, M.-H. Chiu, C.-C. Cheng, C.-W. Yang, K.-H. Wei, Y. Yang *et al.*, Janus monolayers of transition metal dichalcogenides," Nat. Nanotechnol. **12**, 744–749 (2017).
[28]J. Zhang, S. Jia, I. Kholmanov, L. Dong, D. Er, W. Chen, H. Guo, Z. Jin, V. B. Shenoy, L. Shi *et al.*, "Janus monolayer transition-metal dichalcogenides," ACS Nano **11**, 8192–8198 (2017).
[29]L. Dong, J. Lou, and V. B. Shenoy, "Large in-plane and vertical piezoelectricity in Janus transition metal dichalchogenides," ACS Nano **11**, 8242–8248 (2017).
[30]F. Li, W. Wei, P. Zhao, B. Huang, and Y. Dai, "Electronic and optical properties of pristine and vertical and lateral heterostructures of Janus MoSSe and WSSe," J. Phys. Chem. Lett. **8**, 5959–5965 (2017).
[31]Y.-N. Wen, M.-G. Xia, and S.-L. Zhang, "Bandgap engineering of Janus MoSSe monolayer implemented by Se vacancy," Comput. Mater. Sci. **152**, 20–27 (2018).
[32]W. Guo, X. Ge, S. Sun, Y. Xie, and X. Ye, "The strain effect on the electronic properties of the mosse/wsse van der waals heterostructure: A first-principles study," Phys. Chem. Chem. Phys. **22**, 4946–4956 (2020).
[33]M. Idrees, H. Din, R. Ali, G. Rehman, T. Hussain, C. Nguyen, I. Ahmad, and B. Amin, "Optoelectronic and solar cell applications of Janus monolayers and their van der Waals heterostructures," Phys. Chem. Chem. Phys. **21**, 18612–18621 (2019).
[34]H. Din, M. Idrees, A. Albar, M. Shafiq, I. Ahmad, C. V. Nguyen, and B. Amin, "Rashba spin splitting and photocatalytic properties of GeC–M SSe (M = Mo, W) van der Waals heterostructures," Phys. Rev. B **100**, 165425 (2019).
[35]X. Ma, X. Wu, H. Wang, and Y. Wang, "A Janus MoSSe monolayer: A potential wide solar-spectrum water-splitting photocatalyst with a low carrier recombination rate," J. Mater. Chem. A **6**, 2295–2301 (2018).
[36]Z. Guan, S. Ni, and S. Hu, "Tunable electronic and optical properties of monolayer and multilayer Janus MoSSe as a photocatalyst for solar water splitting: A first-principles study," J. Phys. Chem. C **122**, 6209–6216 (2018).
[37]M. Palsgaard, T. Gunst, T. Markussen, K. S. Thygesen, and M. Brandbyge, "Stacked Janus device concepts: Abrupt pn-junctions and cross-plane channels," Nano Lett. **18**, 7275–7281 (2018).
[38]R. Chaurasiya, G. K. Gupta, and A. Dixit, "Ultrathin Janus WSSe buffer layer for $W(S/Se)_2$ absorber based solar cells: A hybrid, DFT and macroscopic, simulation studies," Sol. Energy Mater. Sol. Cells **201**, 110076 (2019).
[39]C. Xia, W. Xiong, J. Du, T. Wang, Y. Peng, and J. Li, "Universality of electronic characteristics and photocatalyst applications in the two-dimensional Janus transition metal dichalcogenides," Phys. Rev. B **98**, 165424 (2018).
[40]J. Wang, H. Shu, T. Zhao, P. Liang, N. Wang, D. Cao, and X. Chen, "Intriguing electronic and optical properties of two-dimensional Janus transition metal dichalcogenides," Phys. Chem. Chem. Phys. **20**, 18571–18578 (2018).
[41]W.-J. Yin, B. Wen, G.-Z. Nie, X.-L. Wei, and L.-M. Liu, "Tunable dipole and carrier mobility for a few layer Janus MoSSe structure," J. Mater. Chem. C **6**, 1693–1700 (2018).
[42]Y. Cai, G. Zhang, and Y.-W. Zhang, "Polarity-reversed robust carrier mobility in monolayer MoS_2 nanoribbons," J. Am. Chem. Soc. **136**, 6269–6275 (2014).
[43]P. Giannozzi, S. Baroni, N. Bonini, M. Calandra, R. Car, C. Cavazzoni, D. Ceresoli, G. L. Chiarotti, M. Cococcioni, I. Dabo *et al.*, "QUANTUM ESPRESSO: A modular and open-source software project for quantum simulations of materials," J. Phys. Condens. Matter **21**, 395502 (2009).
[44]D. Hamann, M. Schlüter, and C. Chiang, "Norm-conserving pseudopotentials," Phys. Rev. Lett. **43**, 1494 (1979).
[45]S. Poncé, E. R. Margine, C. Verdi, and F. Giustino, "EPW: Electron–phonon coupling, transport and superconducting properties using maximally localized wannier functions," Comput. Phys. Commun. **209**, 116–133 (2016).
[46]M. Hosseini, M. Elahi, M. Pourfath, and D. Esseni, "Strain-induced modulation of electron mobility in single-layer transition metal dichalcogenides MX_2 (M = Mo, W; X = S, Se)," IEEE Trans. Electron Devices **62**, 3192–3198 (2015).
[47]P.-F. Chen and Y.-R. Wu, "Calculation of field dependent mobility in MoS2 and WS2 with multi-valley Monte Carlo method," in *2021 International Symposium on VLSI Technology, Systems and Applications (VLSI-TSA)* (IEEE, 2021), pp. 1–2.
[48]Y. Wei, X. Xu, S. Wang, W. Li, and Y. Jiang, "Second harmonic generation in Janus MoSSe a monolayer and stacked bulk with vertical asymmetry," Phys. Chem. Chem. Phys. **21**, 21022–21029 (2019).
[49]A. Kandemir and H. Sahin, "Bilayers of Janus WSSe: Monitoring the stacking type via the vibrational spectrum," Phys. Chem. Chem. Phys. **20**, 17380–17386 (2018).
[50]R. Guo, X. Bu, S. Wang, and G. Zhao, "Enhanced electron–phonon scattering in Janus MoSSe," New J. Phys. **21**, 113040 (2019).
[51]Z. Jin, X. Li, J. T. Mullen, and K. W. Kim, "Intrinsic transport properties of electrons and holes in monolayer transition-metal dichalcogenides," Phys. Rev. B **90**, 045422 (2014).
[52]Y. Ding, G. Yang, Y. Gu, Y. Yu, X. Zhang, X. Tang, N. Lu, Y. Wang, Z. Dai, H. Zhao *et al.*, "First-principles predictions of Janus MoSSe and WSSe for FET applications," J. Phys. Chem. C **124**, 21197–21206 (2020).
[53]K. Kaasbjerg, K. S. Thygesen, and K. W. Jacobsen, "Phonon-limited mobility in n-type single-layer MoS_2 from first principles," Phys. Rev. B **85**, 115317 (2012).
[54]J. Chang, L. F. Register, and S. K. Banerjee, "Ballistic performance comparison of monolayer transition metal dichalcogenide MX_2 (M = Mo, W; X = S, Se, Te) metal-oxide-semiconductor field effect transistors," J. Appl. Phys. **115**, 084506 (2014).
[55]G. Gaddemane, S. Gopalan, M. L. Van de Put, and M. V. Fischetti, "Limitations of *ab initio* methods to predict the electronic-transport properties of two-dimensional semiconductors: The computational example of 2H-phase transition metal dichalcogenides," J. Comput. Electron. **20**, 49–59 (2021).
[56]S.-D. Guo, "Phonon transport in Janus monolayer MoSSe: A first-principles study," Phys. Chem. Chem. Phys. **20**, 7236–7242 (2018).
[57]M. Yang, X. Cheng, Y. Li, Y. Ren, M. Liu, and Z. Qi, "Anharmonicity of monolayer MoS_2, $MoSe_2$, and WSe_2: A raman study under high pressure and elevated temperature," Appl. Phys. Lett. **110**, 093108 (2017).
[58]S.-D. Guo and J.-T. Liu, "Lower lattice thermal conductivity in SbAs than As or Sb monolayers: A first-principles study," Phys. Chem. Chem. Phys. **19**, 31982–31988 (2017).
[59]G. Zheng, Y. Jia, S. Gao, and S.-H. Ke, "Comparative study of thermal properties of group-VA monolayers with buckled and puckered honeycomb structures," Phys. Rev. B **94**, 155448 (2016).
[60]S. Wang, W. Wang, and G. Zhao, "Thermal transport properties of antimonene: An *ab initio* study," Phys. Chem. Chem. Phys. **18**, 31217–31222 (2016).

[61]Z. Qin, G. Qin, X. Zuo, Z. Xiong, and M. Hu, "Orbitally driven low thermal conductivity of monolayer gallium nitride (GaN) with planar honeycomb structure: A comparative study," Nanoscale **9**, 4295–4309 (2017).
[62]H. Liu, Z. Huang, C. He, Y. Wu, L. Xue, C. Tang, X. Qi, and J. Zhong, "Strain engineering the structures and electronic properties of Janus monolayer transition-metal dichalcogenides," J. Appl. Phys. **125**, 082516 (2019).
[63]S.-D. Guo and J. Dong, "Biaxial strain tuned electronic structures and power factor in Janus transition metal dichalchogenide monolayers," Semicond. Sci. Technol. **33**, 085003 (2018).
[64]G. Gaddemane, W. G. Vandenberghe, M. L. Van de Put, E. Chen, and M. V. Fischetti, "Monte-Carlo study of electronic transport in non-σ h-symmetric two-dimensional materials: Silicene and germanene," J. Appl. Phys. **124**, 044306 (2018).